Icarus 396 (2023) 115503

Contents lists available at ScienceDirect

Icarus

journal homepage: www.elsevier.com/locate/icarus

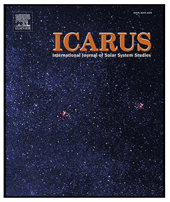

Research Paper

Experimental study of frost detectability on planetary surfaces using multicolor photometry and polarimetry☆

Stefano Spadaccia *, C.H. Lucas Patty, Nicolas Thomas, Antoine Pommerol

Space Research and Planetary Sciences Division, Physikalisches Institut, University of Bern, Sidlerstrasse 5, Bern, 3012, Switzerland

ARTICLE INFO

Dataset link: https://doi.org/10.5281/zenodo.7681502

Keywords:
Comets, composition
Ices
Experimental techniques
Mars, surface
Polarimetry
Photometry

ABSTRACT

When the temperature and pressure conditions allow it, water ice can deposit as frost on the regolith of planetary surfaces. Frost is an important indicator of the surface physical conditions, and may trigger geological processes by its deposition and sublimation. This works aims to explore, experimentally, the possibility of detecting early stages of frost formation and to characterize its spectrophotometric and spectropolarimetric signatures in visible reflected light. We deposit ice on top of different regolith simulants, measuring the dust temperature, the thickness, and the morphology of the frost through a microscope, while measuring the reflected light at phase angles of 50° and 61°, and the linear polarization at phase angles of 5° and 16°, at three different wavelengths (450, 550, and 750 nm). We show that both the spectral slope (in particular between 450–550 nm), and the difference of polarization between 450 and 750 nm are efficient methods to detect frost layers with thicknesses as low as 10 to 20 μm. Furthermore, we find that the linear polarization at 16° relates to the temperature of the regolith i.e. the type of the deposited ice crystalline structure.

1. Introduction

Water ice is ubiquitous in our Solar System and frequently seen on planetary surfaces. Ice in the Solar System can assume many configurations: enclosed in thick polar ice sheets (as on Earth and Mars), as thin frost layers on objects where the day–night temperature difference allows ice deposition, intermixed with dust and organic material (as in the case of comets), as tiny ice crystals in clouds of different planets (Earth, Mars, Jupiter), and finally it is also found in interplanetary dust particles. The observation of water ice on surfaces of the Solar System bodies helps trace their present and past geological processes, but also helps understand how water ice distributed among those bodies during the Solar System formation and evolution (Blum et al., 2022). The deposition of thin layers of water ice crystals (referred to in this study as "frost") on dusty surfaces is important for minor bodies and planetary surfaces. We distinguish frost from more compact, thick, sintered, slab-like icy surfaces. Monitoring the frost formation informs us about the diurnal and seasonal water cycles of such bodies, providing important information on how the ice interacts with planetary surfaces and changes their physical properties.

The superficial water ice on Solar System bodies can be detected by water absorption bands in the near infrared (NIR) and infrared (IR) positioned at 1.05, 1.25, 1.5, 2.0, and 3.2 μm, which are very distinctive and diagnostic of the presence of pure water ice. Nonetheless, when ice is mixed with low-albedo materials (such as dark asteroid or comet regolith), its NIR absorption bands can become shallower, or disappear completely (Clark, 1981; Roush et al., 1990; Pommerol et al., 2019; Raponi et al., 2016). Another way to detect ice is through color differences of the scattered light in the visible range. In general, dust in our Solar System has a higher reflectance in the red than in the blue, translating into a positive slope of its visible spectrum. Since the visible spectrum of ice is flat or slightly more reflecting in the blue (at least for smaller particle sizes), the spectral slope in the range ~400 to 800 nm can be indicative of water ice on the surface. On comets 9P/Tempel 1, 103P/Hartley 2 and 67P/Churyumov–Gerasimenko (67P hereafter), decreases in spectral slopes in the 400 to 800 nm range have been associated with the presence of surface ice (Fornasier et al., 2015; Li et al., 2007, 2013), and the "blueing" effect of ice has been confirmed through experimental studies (Pommerol et al., 2015). On minor bodies, both the deposition and sublimation of ice are extremely important processes that change the morphology of the surface, its spectra and other physical properties such as porosity, compressive strength, and thermal conductivity. Ice deposition and sublimation have been observed at the surface of 67P, in shadowed regions showing an increase of albedo and higher blue slopes when illuminated, and

☆ This work has been carried out within the framework of the National Centre of Competence in Research PlanetS supported by the Swiss National Science Foundation under grants 51NF40_182901 and 51NF40_205606. The authors acknowledge the financial support of the SNSF, Switzerland.

* Corresponding author.
E-mail address: stefano.spadaccia@unibe.ch (S. Spadaccia).

https://doi.org/10.1016/j.icarus.2023.115503
Received 5 December 2022; Received in revised form 27 February 2023; Accepted 28 February 2023
Available online 1 March 2023

becoming darker and redder a few minutes afterwards (De Sanctis et al., 2015; Fornasier et al., 2016; Liao et al., 2018). The spectra and thermal modeling of such frost seem to indicate that the ice is inter-mixed with the dust particles and up to 15 μm thick (Fornasier et al., 2016).

The presence of permanent superficial frost on some asteroids is still debated (Yang and Jewitt, 2007). While the presence of sub-surface ice is plausible for many main-belt asteroids (Schorghofer, 2016), icy patches or frost on the surface would be rapidly lost due to the sublimation rates at those heliocentric distances. Nonetheless, observations of 24-Themis and 65-Cybele have revealed an absorption band at 3.1 μm that is consistent with surface water ice and organic material (Campins et al., 2010; Rivkin and Emery, 2010; Licandro et al., 2011). Jewitt and Guilbert-Lepoutre (2011) did not find any spectroscopic emission lines associated with water ice sublimation on 24-Themis and 65-Cybele, and proposed that the surface ice must have been a transient event due to impacts that blanketed these bodies with a thin layer of ice. While ice could be locally present on these asteroids, O'rourke et al. (2020) found that the modeled upper limits of water out-gassing are not compatible with the observed 3.1 μm absorption band, and other minerals have been proposed to cause the absorption feature at 3.1 μm (Beck et al., 2011). Still, addressing the presence of thin films of ice on planetary surfaces remains problematic.

Polarization is a powerful observational technique used to characterize the properties of the dust on the surfaces of different bodies in our solar system. The polarization of the solar light scattered by a planetary surface provides useful insights on the composition, size, morphology, and porosity of the regolith particles. The linear polarization is defined as

$$P = \frac{I_\perp - I_\parallel}{I_\perp + I_\parallel}, \tag{1}$$

where $I_\perp$ and $I_\parallel$ are the differences in intensities of the reflected light after filtering the polarization at perpendicular directions, respectively normal and parallel to the plane of scattering. Note that $P = Q/I$ using the formulation of the Stokes parameters. P varies depending on the angle between the observer, the observed object, and the illumination source, called phase angle α. The linear polarization of an astronomical body depending on the phase angle is called polarization phase curve. Polarization phase curves have been used extensively to investigate the properties of the Moon regolith (Dollfus, 1998), of asteroid surfaces (Belskaya et al., 2017; Cellino et al., 2015; Belskaya et al., 2019), and cometary comae (Levasseur-Regourd et al., 2018). When unpolarized light shines on these objects for phase angles about $\alpha < 25°$, P is negative, i.e. $I_\perp < I_\parallel$. This part of the polarization phase curve is often called negative polarization branch or negative polarization (NP). The NP shape is determined by the minimum of polarization P_{min} and the phase angle at which the polarization goes back to zero, called the inversion angle α_{inv} (see Fig. 8 as an example). These two parameters vary significantly depending on the scattering regime of the observed dust: in the case of single scattering (e.g. cometary comae) the inversion angle is larger and $|P_{min}|$ is higher than in the case of multiple scattering (regolith and planetary surfaces). This is due to the fact that multiple scattering contributes to the scrambling of the polarization direction, decreasing the overall net polarization escaping the medium. The minimum of polarization can change significantly depending on the phase curve, but in general it lies in the range P_{min} = 0.2–2% for asteroids and cometary comae. The inversion angle can also change depending on the physical properties of the observed dust: its value lies in the range α_{inv} = 14–28° for asteroids and about α_{inv} = 22° for comets. Modeling the observed NP both experimentally and theoretically can provide constraints on the particle size distribution, porosity, and mineralogy (Shkuratov et al., 2002; Zubko et al., 2013; Frattin et al., 2019; Spadaccia et al., 2022).

Frost and small icy particles have a distinctive polarization signal in reflected light, that makes polarization an interesting tool for detection and analysis of their properties. In the literature, a limited number of studies are available on the polarizance of frost. The first pioneering measurements of frost polarization phase curves were carried out by Dollfus (1957), who observed low polarization values and curve variability depending on the melting state of the frost. Steigmann (1993) was the first studying frost-dust associations, demonstrating that Callisto polarization phase curve at small angles (negative polarization) could be reproduced by sprinkling different types of silicate dust on top of a frost layer. The crystal size of frost or snow influences the polarization signal too — snow crystals with sizes in the range up to 900 μm show low negative polarization, that is dependent to some degree on the grain size (Shkuratov and Ovcharenko, 2002; Lv and Sun, 2014). More recently, Poch et al. (2018) studied how the phase polarization curves of small spherical icy particles and frost change over time due to sintering and frost growth. They discovered that frost deposition seems to cause multiple local minima to the polarization phase curve, which they attributed to Mie scattering of the first hemispherical nucleation sites of the frost. All these works studied frost deposition either at one single wavelength or of pure ice on a metal substrate, and more comprehensive pectropolarimetry studies of frost forming on regolith simulants are lacking in the literature.

In this work, we explore the possibility of detecting early-formation of water frost on dusty surfaces through observation of both total and polarized reflected light in different wavelengths and phase angle configurations. Furthermore, we correlate the total reflected light and polarization variations over time with the frost thickness and physical properties. Frost is formed on two different regolith surfaces: the Martian Global Simulant MGS-1 (Cannon et al., 2019) and the CR Carbonaceous Chondrite Simulant (Britt et al., 2019). The asteroid simulant is cooled down to −150 °C (about 120–130 K), consistent with the surface temperature of asteroids such as (1) Ceres at mid-high latitudes (Rivkin and Emery, 2010). The martian simulant was cooled either at −130 °C or −100 °C that are lower than the mean water frost point on Mars (183–193 K) and are consistent with the low temperatures of polar-facing martian slopes (Schorghofer and Edgett, 2006).

This work is structured as follows: in Section 2 we present our experimental methods and apparatus, in Section 3 we summarize our findings, in Section 4 we provide a discussion of the results in the context of frost detectability through total and polarized reflected light. We finally present future perspective and experiments in Section 5, and we conclude in Section 6.

2. Materials and methods

In this section, we describe the experimental setup used for the frost deposition, and we give details about the photopolarimetry measurement procedure.

2.1. Experimental setup description

We used the POLarimeter for ICE Samples (POLICES) developed at the University of Bern (Spadaccia et al., 2022; Poch et al., 2018; Patty et al., 2022), which is schematically depicted in Fig. 1. The POLICES full Stokes polarimeter (Dual PEM II/FS42-47, Hinds Instruments) consists of 2 PEMs oriented at 45° modulated at 42 and 47 kHz resonance frequencies, a prism analyzer that is 22.5° to the PEMs and a photomultiplier tube (Hamamatsu 6/37 R955, Japan) (Patty et al., 2022). The polarimeter performance was validated against the results of a rotating polarizer in transmission, with a resulting polarimetric sensitivity of 10^{-4}. The polarimeter is positioned on top of a trapezoidal enclosure, with the entrance pupil exactly above and perpendicular to the sample. The light source is a 250 W halogen lamp which feeds a monochromator (Quantum Design MSH-300) placed outside the enclosure. The output light is collected by an optical fiber entering the enclosure. A motorized arm holds the optical fiber that sends a collimated beam of light to the sample with a spot diameter of approximately 15 mm. To ensure

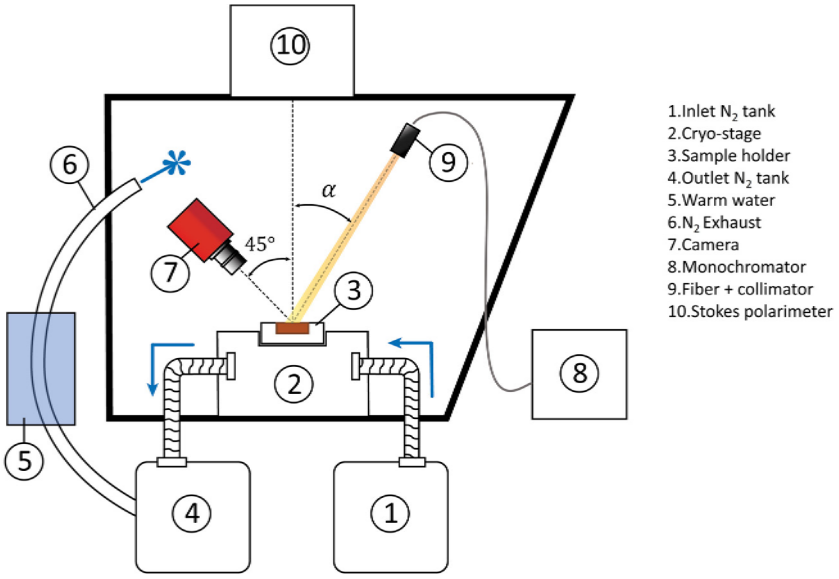

Fig. 1. Schematics of the POLICES setup for measuring the polarization and total intensity of cryogenic samples.

unpolarized incident light, a liquid-crystal depolarizer was placed between the monochromator and the optics converging into the fiber launcher. In this way, the incidence light on the sample has less than 10^{-4} remnant polarization at 450–750 nm, which agrees well with the polarization of the global light coming from the solar disk (Kemp et al., 1987). The arm can assume any position between 2° and 70°, changing the incidence angle of the illumination, while the polarimeter measures the reflected light at 0° (in this configuration, the incidence angle has the same value as the phase angle). To measure the total reflected light, we used a monochromatic camera (Thorlabs Kiralux CMOS CS126MU) placed at 45° with respect to the sample surface, on the opposite side of the motorized arm. The wavelength of the incident light can be selected with the monochromator, with a full width at half maximum of 35 nm. The regolith sample is accommodated in a cylindrical volume carved in an aluminum sample holder, with a diameter of 3.5 cm and depth of 5 mm. The aluminum sample holder is placed on top of the cryo-stage that consists of a copper cylindrical volume equipped with two pipes (inlet and outlet) connected to two liquid nitrogen tanks. The first tank is full of liquid nitrogen and thus has a higher pressure than the second one, which is empty. When the valve of the inlet pipe is open, the nitrogen flows inside the copper volume actively cooling it down, and the exhaust nitrogen flows into the second tank. The exhaust valve of the second tank is fully open and connected to a pipe that goes back in the POLICES enclosure. When the nitrogen flows in the second tank that is at ambient pressure and temperature, it evaporates and escapes from the exhaust valve in the pipe and finally into the enclosure. This allows the chamber to be flushed with gaseous nitrogen. To avoid the gaseous nitrogen being too cold, the pipe is immersed in a warm water bath before entering the enclosure.

The experiments consist of measuring the Stokes parameters at two fixed phase angles sampling the minimum and the inversion angle of the negative polarization phase curve (α = 5° and 16°) at three wavelengths (450 nm, 550 nm, and 750 nm) of regolith simulants cooled to low temperatures. At the same time, the total light intensity at the three wavelengths is independently measured by a camera placed at 45° with respect to the sample surface (i.e. the intensity is measured at a phase angle of 50° and 61°). The intensity measurements are calibrated using a 75% spectralon target. The camera is defocused, so that the observed illuminated spot is spatially averaged, and the reflectance is then calculated over a region of interest within the light spot. Defocusing the objective of the camera prevents to resolve the fine structure of the sample and eventual heterogeneity of the frost deposition.

Finally, we repeated the experiment with the different regolith types (see Section 2.2) observed with a long-distance microscope (K2 DistaMax) and illuminated by broadband incident light. The images from the microscope were used to measure the frost thickness and growth.

2.2. Samples and experimental procedure

The two regolith simulants used in our experiment are the Martian Global Simulant MGS-1 (Cannon et al., 2019) and the CR Carbonaceous Chondrite Simulant (Britt et al., 2019). Both simulants appear quite dark in the visible: the MGS-1 reflectance is about 11% at 450 nm and reaches 24% at 750 nm, while CR is about 4% at 450 nm and about 7% at 750 nm (Fig. 2A and B). A scanning electron microscope (SEM) inspection of the simulants reveals that part of their mass is composed of fine powder with grain sizes less than 5 μm (Fig. 2C and D).

We sieved the simulants to remove grains and aggregates bigger than 2 mm and then we placed the regolith inside the carved volume of the sample holder to obtain a flat surface without compressing the sample. A Pt100 resistance thermal sensor was placed inside the regolith layer to measure its temperature during the experiment, at approximately 2–3 mm from the regolith surface. The sample holder was then placed on top of the cryo-stage. A good thermal contact between the cryo-stage and the aluminum sample holder was assured by a piece of graphite sheet. Before cooling down the cryo-stage, the aluminum sample holder is covered by an aluminum lid to prevent frost depositing on the sample before the target temperature is reached. At this point, we opened the first tank inlet valve, flowing liquid nitrogen in the cryo-stage that starts cooling down. At the same time, the exhaust gaseous nitrogen flows from the second tank to the enclosure, rapidly flushing the chamber. Shortly before the regolith reached the target temperature, we removed the aluminum lid over the sample through a glove hermetically sealed on one side of the enclosure, and started the polarization and intensity measurements.

The data acquisition steps were the following. The motorized arm moves to the first target phase angle (α = 5°), then the monochromator selects the 450 nm wavelength, and we measure the Stokes parameters. Afterwards, the camera acquires the image in total light. Then, the other two wavelengths (550 and 750 nm) are selected successively and the polarization and intensity data are acquired in the same way. Finally, the motorized arm moves to α =16° and the whole procedure is repeated. The data acquisition for the two phase angles and the three wavelengths takes 3 min.

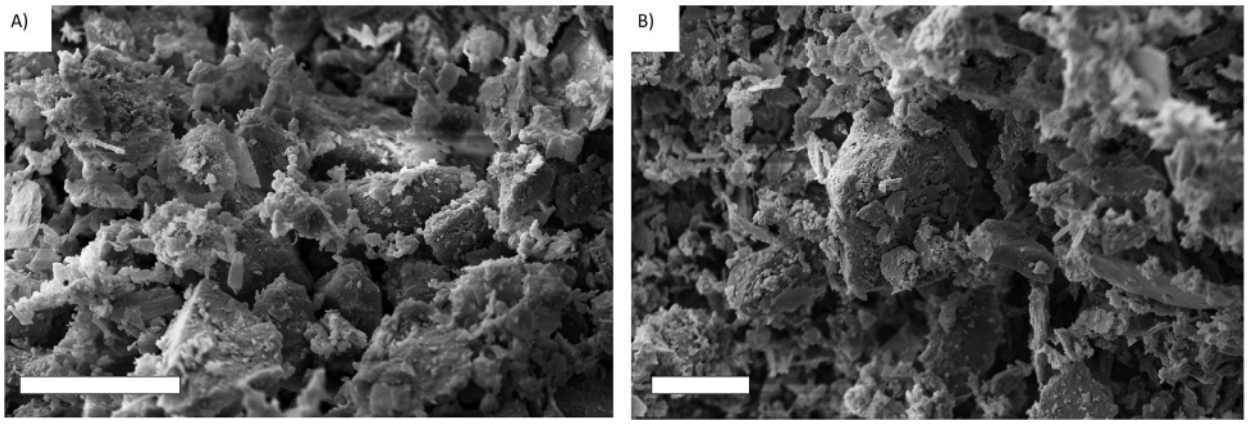

Fig. 2. Spectra of the MGS-1 (in brown, plot A) and of the CR simulants (in brown, plot B). The spectra are from Britt et al. (2019) and Cannon et al. (2019). (C) SEM image of MGS-1 and (D) CR. The scale bar is 20 μm for both SEM images.

After the acquisition of the polarization and reflection data at all wavelengths for both phase angles, the exhaust pipe is removed from the chamber and the inlet nitrogen valve of the first is closed. The cryo-stage still contains liquid nitrogen and continues to cool down for about 10–20 min (depending on the final temperature reached), until the liquid nitrogen evaporates completely and goes out through the outlet toward the second tank. At this point, the temperature of the cryo-stage starts to increase. The measurements continue until a thick layer of frost has formed on the sample, usually between 80 and 140 min after the beginning of the experiment (depending on the final temperature).

From the reflectance data, we can derive the spectral slope in %/100 nm between two wavelengths λ_2 and λ_1 (with $\lambda_2 > \lambda_1$)

$$S(\lambda_1, \lambda_2) = \frac{R_{\lambda_2} - R_{\lambda_1}}{R_{\lambda_1}\left(\lambda_2 - \lambda_1\right)}. \quad (2)$$

following the definition introduced by Delsanti et al. (2001), and used to interpret 67P spectrophotometric data by Fornasier et al. (2015, 2016).

3. Results

Here we present the averaged photometric and polarimetric results from five experiments with the CR simulant, three experiments with the MGS-1 simulant cooled down to −130 °C (hereafter called cold-case) and three experiments with the MGS-1 cooled at −100 °C (hereafter called hot-case). Furthermore, for both simulants under all temperature conditions, we performed one separate experiment with the long-distance microscope to observe the frost formation and measure its thickness. The reflectance and polarization results are the average of the experimental repetitions. The variability between different experimental repetitions is due to slight changes of frost deposition rate, which can cause increasing standard deviations over time (see Figs. 4, 5, 6).

Since the difference of the spectral slopes between phase angles $\alpha = 50°$ and $\alpha = 66°$ is within 1%, we show only the spectral slopes measured at $\alpha = 50°$. Since the lower limit of frost thickness detection is limited by the microscope resolution, the frost thickness in the first minutes of experiment is extrapolated from the measured data through polynomial fitting.

3.1. Frost growth and temperature conditions

The temperatures of CR and the MGS-1 (cold and hot case) are presented in Fig. 3. The long-distance microscope acquired one image every three minutes, starting when the cooling of the cryo-stage is turned off and the nitrogen exhaust pipe is removed from the POLICES enclosure. The images were compared to each other, and we measured the thickness of frost in different areas of the image to get an average and a standard deviation. High values of standard deviation come from the appearance of big single ice crystals localized on top of bigger dust grains.

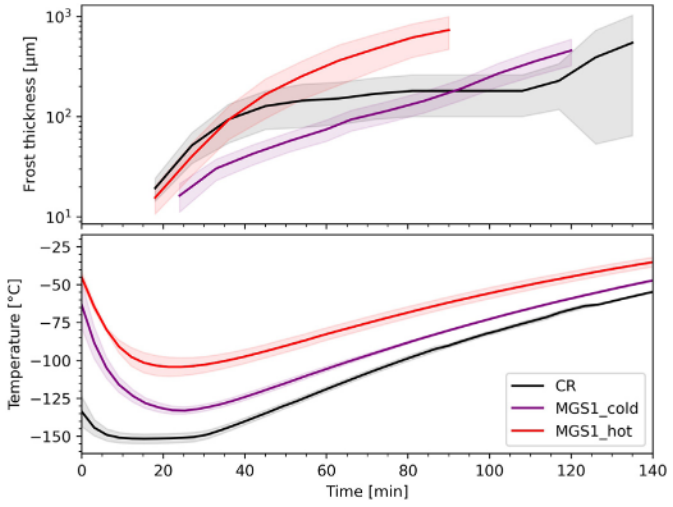

Fig. 3. On top, result from the long-distance microscope measurements of frost thickness with CR and MGS-1 (cold and hot case). The shadowed areas around the curves indicate the standard deviation of at least ten measurements in different parts of the image. At the bottom is the average temperature of the experiments. The shadowed areas around the curves represent the standard deviation of the experiment repetitions. (For interpretation of the references to color in this figure legend, the reader is referred to the web version of this article.)

The temperature at which the frost deposits on top of the simulant plays an important role. Counterintuitively, the MGS-1 grows frost faster when it is warmer. This effect is due to the fact that the air on top of the cryo-stage is cooled by conduction, and the colder the air, the less water vapor it can contain. Furthermore, there is a compositional difference between CR and MGS-1. Ice deposition is different for different materials, since the vapor partial pressure needed to trigger the nucleation of ice depends on the substrate material (Iraci et al., 2010). In our case, we observe that deposition of frost on CR simulant is faster than MGS-1, although its temperature is lower.

3.2. Multicolor polarimetry and photometry of frost

In this section, we present the multicolor polarimetric and photometric results during the frost deposition process. The CR simulant is

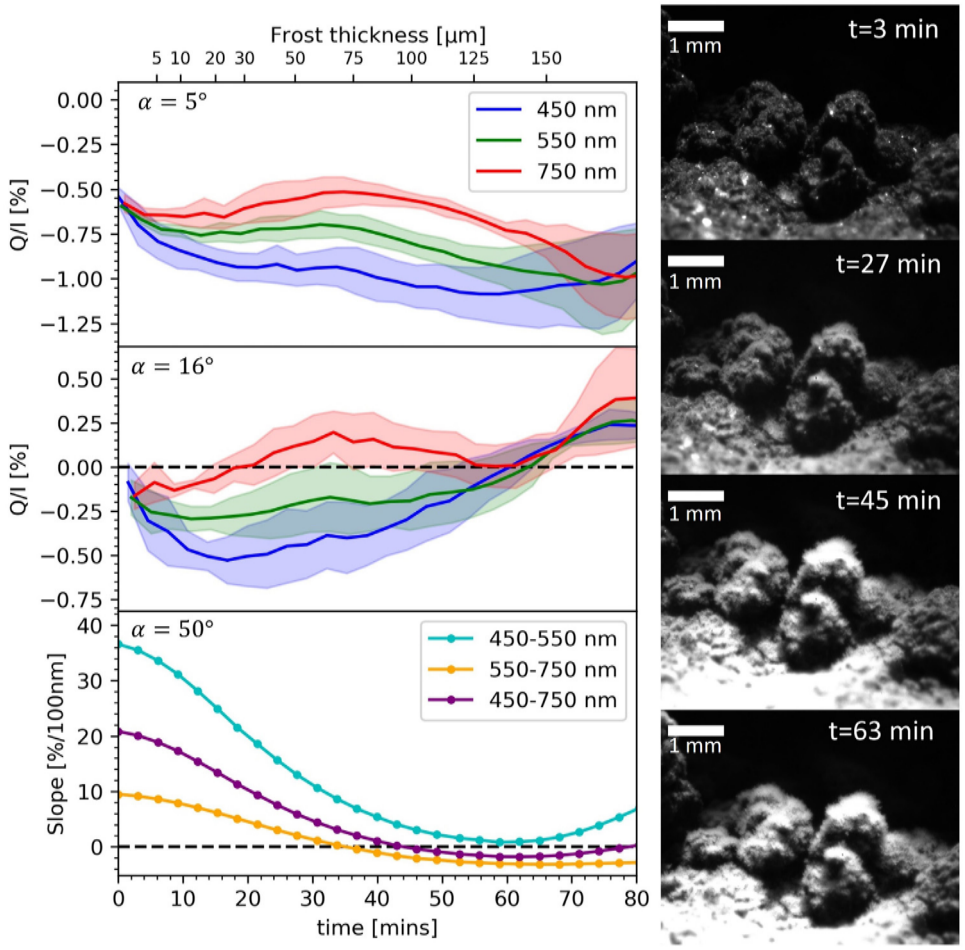

Fig. 4. The evolution of the linear polarization at 450, 550 and 750 nm at phase angle of $\alpha = 5°$ (top graph), $\alpha = 16°$ (middle graph), spectral slope (bottom graph), and frost thickness (top bar) on CR regolith simulant. The shaded areas around the polarization measurements are the standard deviation of the five experiment repetitions. The slope is calculated using Eq. (2) with wavelengths 450–550, 550–750 and 450–750 nm. The images of the regolith sample show the deposition of frost on the surface at different times (right), the scale bar is 1 mm. (For interpretation of the references to color in this figure legend, the reader is referred to the web version of this article.)

cooled down to T= −150 °C and during the first 10 min of experiment it deposits approximately 10 μm of frost. At the beginning of the experiment, the linear polarization at 5° and 16° show approximately the same value in the three wavelengths ($P = -0.6\%$ and $P = -0.2\%$, respectively). After about 10 min (i.e. 10 μm of frost), P at 450 nm (P_{450}) decreases to $P_{450} = -0.85\%$ and it is well distinguished from the values at the other two wavelengths. The separation of P between the three wavelengths continues until the frost become between 125 and 150 μm-thick, then the three channels return to the same P values within the uncertainties. The maximum difference between blue and red linear polarization $|P_{450} - P_{750}| = 0.4\%$ is reached at 5° when the frost thickness is 50 – 100 μm, and at 16° when the frost thickness is 50 μm. The spectral slope diminishes over time toward negative values. Because of its definition (see Eq. (2)), the spectral slope is higher when $\lambda_1 = 450$ nm, than when $\lambda_1 = 550$ nm. The spectral slope $S_{450–750}$ decreases by 10% already at 15 min, when the frost is 14 μm thick. We can observe that CR undergoes a plateau phase in the frost crystal growth when it reaches approximately 100 μm thickness (Fig. 3).

In the first 20 min, the MGS-1 cools down to T= −130 °C ("cold-case"), and then its temperature evolves slowly back to T= −90 °C 80 min after the beginning of the experiment (Fig. 3). The frost deposition rate is slower than the "hot-case" MGS-1 or CR. Since MGS-1 is more reflective in the red than in the blue, the reflectance is higher at 750 nm, and, as a direct consequence, the linear polarization at small angles is lower in the red than in the other channels (see the linear polarization at $\alpha = 5°$ in the top plot of Fig. 5). The linear polarization close to the negative polarization minimum (at $\alpha = 5°$) is evolving in the same way as CR: $|P_{450}|$ already increases when the frost is 10 μm thick, and the maximum separation from the red channel happens at ~20 μm frost thickness, $|P_{450} - P_{750}| = 0.5\%$. At 16°, the three channels evolve mostly together, and it is worth noting that P_{450} and P_{550} become negative with frost thicknesses between 10 and 20 μm. For both phase angles, the channels converge at 50–60 min from the beginning of the experiment, when the frost thickness exceeds 50 μm thickness, and starts looking as a white blanket over the simulant grains. The spectral slopes between 450–550 nm and 450–750 nm differ of 2–4%, and they decrease by approximately 10%/100 nm during the first 20 min, when the frost thickness is approximately 15 μm, while the spectral slope at 550–750 nm decreases by the same amount in slightly more time (24 min i.e. approximately 20 μm of frost).

The second experiment with MGS-1 was performed at higher temperatures ("hot-case"). The minimum temperature reached by the simulant was T= −100 °C after about 20 min from the beginning of the experiment. The frost deposition rate is higher compared to the cold-case throughout the whole experiment duration (Fig. 3, red curve). The polarimetric behavior also shows some differences compared to the MGS-1 cold-case (Fig. 6). At 5°, the linear polarization in the blue and in the other two channels deviates only after 13 μm of frost, reaching a maximum $|P_{450} - P_{750}| = 0.5 \pm 0.1\%$ (to be compared with the difference at the beginning of the experiment, $|P_{450} - P_{750}| = 0.2\%$). At 16° linear polarization it is the same for the three wavelengths at the beginning of the experiment, but P_{450} rapidly evolves toward

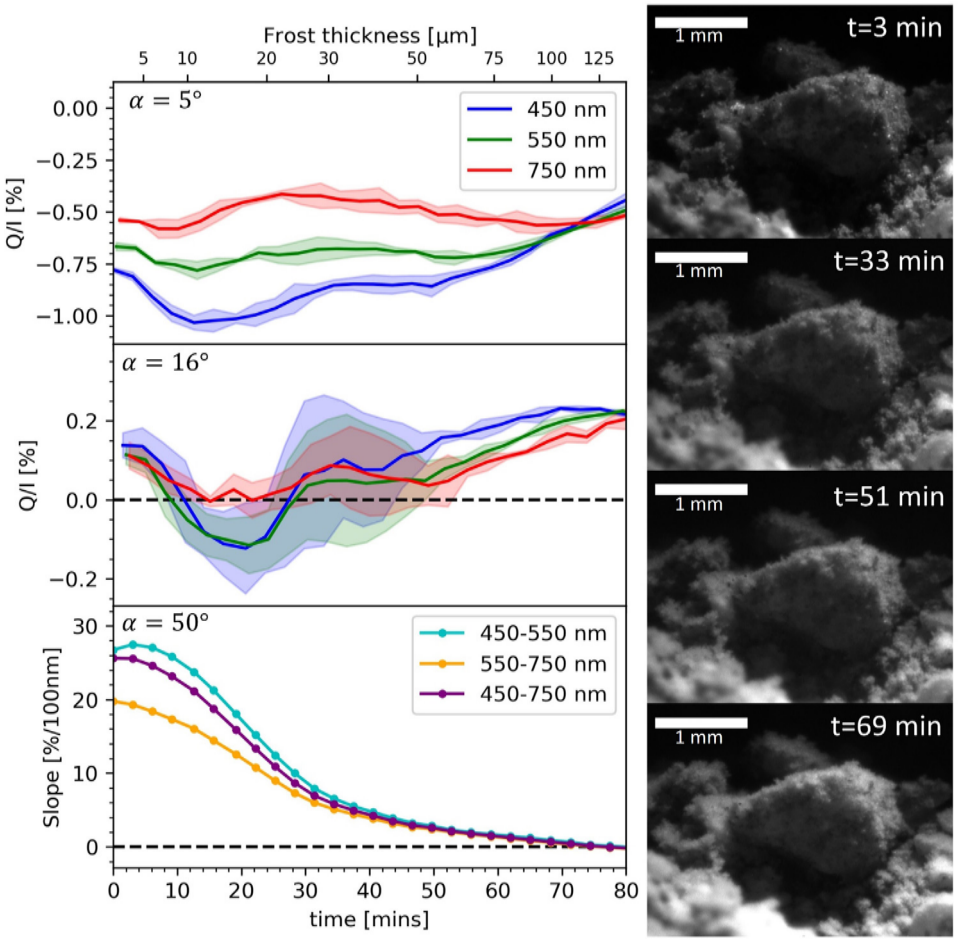

Fig. 5. The evolution of the linear polarization at 450, 550 and 750 nm at phase angle $\alpha = 5°$ (top graph), $\alpha = 16°$ (middle graph), spectral slope (bottom graph), and frost thickness (top bar) on MGS-1 simulant in the cold case. The shaded areas around the polarization measurements are the standard deviation of the three experiment repetitions. The slope is calculated using Eq. (2) with wavelengths 450–550, 550–750 and 450–750 nm, the phase angle is $\alpha = 50°$. The images of the regolith sample show the deposition of frost on the surface at different times (top right). The scale bar represents 1 mm. (For interpretation of the references to color in this figure legend, the reader is referred to the web version of this article.)

positive values, reaching a maximum $P_{450} = 0.45\%$ at 17 min. At this time, the difference between linear polarization in the red and in the blue is $|P_{450} - P_{750}| = 0.3\%$, and the frost thickness is 14 μm. The spectral slope behavior is very similar to the cold-case MGS-1. The first two data points show an increase of reflectance in the green channel ($S_{450–550}$ increases by about 1.5%) and then the evolution is similar to the spectral slopes of CR and colder MGS-1. Both $S_{450–550}$ and $S_{450–750}$ decrease by 10%/100 nm when the frost thickness is 20 μm, while $S_{550–750}$ decreases by the same amount once the frost reaches approximately 30 μm thickness. Since the frost growth is faster than for CR and cold MGS-1, after only 60 mins the frost develops its characteristic dendritic crystals with sizes as large as 250 μm. When the ice crystals grow to this size, their spectral slope is practically zero for all three wavelengths, and the polarization signal is indistinguishable in the three channels.

We can draw some general concluding remarks on the visible multicolor photometric and polarimetric appearance of frost growth and evolution on different substrates based on these observations:

- When frost is observed at angles close to the minimum of the negative polarization curve (in our case 5°), the linear polarizations in the blue, green and red deviates from each other, with the maximum difference reached by the blue and the red channels $|P_{450} - P_{750}|$ in the range $0.25 - 0.5\%$ when the frost thickness is $10 - 20$ μm. When the frost is more mature and the ice crystals size exceeds 100 μm, the linear polarization decreases without color differences.
- At phase angles close to the inversion angle (in our case 16°), the wavelength separation in linear polarization appears in the case of CR and hot MGS-1 ($|P_{450} - P_{750}| = 0.4 \pm 0.2\%$), but it is not detectable in the cold MGS-1 ($|P_{450} - P_{750}| = 0.10 \pm 0.09\%$). Interestingly, there is a strong difference between the blue linear polarization of cold MGS-1 ($P_{450} = -0.1\%$) and hot MGS-1 ($P_{450} = +0.45\%$) when frost is 15 μm thick.
- The spectral slopes decrease significantly when the frost thickness reaches ~20 μm thickness. The spectral slope between 450 and 550 nm changes faster than the others depending on the frost size. On the other hand, the spectral slope between 550 and 750 nm shows shallower behavior and slower changes with frost thickness.

4. Discussion

We performed laboratory experiments to study the evolution of a regolith-like material when frost deposits on its surface at low temperatures, in reflected polarized and total light at different wavelengths and phase angles. Our experiments showed that a layer of frost depositing on a regolith sample can be detected already when the ice layer is 10 μm thick.

4.1. Frost thickness and multicolor photometry

The *Rosetta* mission allowed us to observe in detail the surface of 67P nucleus, and detect water ice patches (Pommerol et al., 2015)

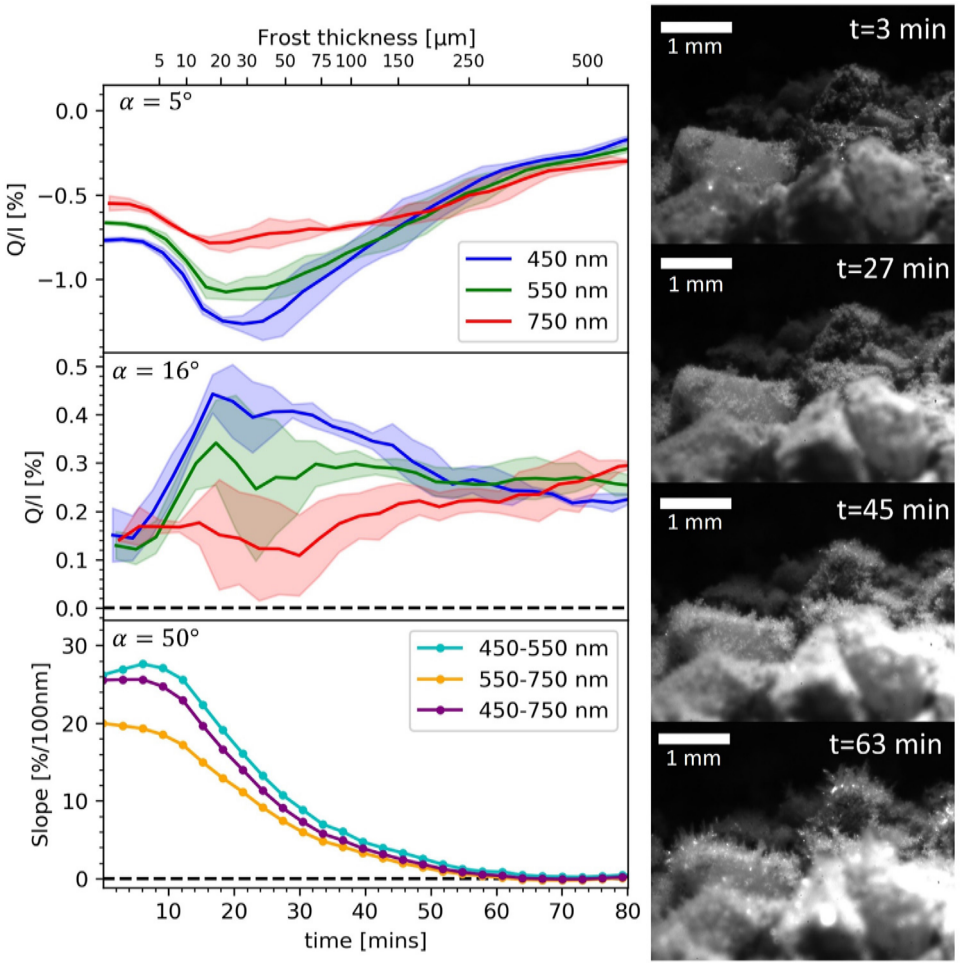

Fig. 6. The evolution of the linear polarization at 450, 550 and 750 nm at phase angle $\alpha = 5°$ (top graph), $\alpha = 16°$ (middle graph), spectral slope (bottom graph), and frost thickness (top bar) on MGS-1 simulant in the hot case. The shaded areas around the polarization measurements are the standard deviation of the three experiment repetitions. The slope is calculated using Eq. (2) with wavelengths 450–550, 550–750 and 450–750 nm, the phase angle is $\alpha = 50°$. The images of the regolith sample show the deposition of frost on the surface at different times (right), the scale bar represents 1 mm. (For interpretation of the references to color in this figure legend, the reader is referred to the web version of this article.)

and frost (De Sanctis et al., 2015; Fornasier et al., 2016, 2019, 2021). Previously, bright spots of water ice had been already observed on the surface of the comet 9P/Tempel 1 (Sunshine et al., 2006) and comet 103P/Hartley 2 (A'Hearn et al., 2011). Although no spectral slope data were produced for the icy spots on these two comets, they have been correlated to water ice absorption bands and to an increase in reflectance at shorter wavelengths. Fornasier et al. (2016) detected daily color variations on the surface of 67P in the Imhotep region with 0.5% uncertainty. These changes are possibly due to nighttime water frost deposition that disappears shortly after illumination of the Sun. The frost fringes appear about six times brighter than the average comet reflectance, and disappear after a few minutes of illumination. The spectral slope of the fringes calculated between 535–882 nm is approximately 12%/100 nm, and it increases to 16%/100 nm in about 40 min. From the thermal model of the surface, Fornasier et al. (2016) estimated the sublimation rate of the water ice, retrieving a 10–15 μm of frost thickness. We can attempt to compare the 535–882 nm color variation observed on 67P to the closest spectral slope calculated in our experiments (550–750 nm). While the albedo of 67P is closer to the reflectance values of CR, its visible spectrum is redder, with spectral slopes in ice-free areas of approximately $S_{535–882}$ = 16–20%/100 nm (this value depends on the heliocentric distance, with lower values at perihelion, and on the phase angle). Such a value lies between the frost-free spectral slope of CR and MGS-1 simulants, $S_{550–750}$ = 10%/100 nm and $S_{550–750}$ = 20%/100 nm, respectively. In both cases, a decrease of $\Delta S_{550–750}$ = 4%/100 nm is equivalent to a frost thickness in the range 10–20 μm. This result is in agreement with the thickness estimated by Fornasier et al. (2016) derived from the ice sublimation rate. In the Anhur region, Fornasier et al. (2019) detected long-lasting water frost in shadowed areas, with the spectral slope decreasing from $S_{535–882}$ = 18%/100 nm to $S_{535–882}$ = 3–10%/100 nm at 87° phase angle. The phase angle of our experiment is lower (maximum 66°) than the phase angle of this observation. Nonetheless, such small spectral slope values are in agreement with thick layers of frost (up to 75–150 μm). These results demonstrate that water frost is detectable already when it is 10 μm thick, by tracking the color changes of a surface. The observation of color changes at shorter wavelengths should provide an advantage in detecting thinner layers of frost, because of the sensitive response in blue caused by water ice deposition.

There are only a few observations of water frost on Mars. In 1977, *Viking 2* detected H_2O forming at nighttime at 48°N and disappearing a few minutes after sunrise (Jones et al., 1979; Svitek and Murray, 1990). In 2008, the space probe *Phoenix* excavated some trenches in the Mars soil at 68°N and found a consolidated slab of subsurface water ice and more porous, pure underground patches of ice. Later on, it detected frost forming at nighttime on the landing site surface (Smith et al., 2009). Carrozzo et al. (2009) used the OMEGA imaging spectrometer near-infrared data on board of *Mars Express* and successfully detected water frost on shadowed slopes at low latitudes (between 30°S and 12°N). In the northern hemisphere (between 12°S and 30°N), frost was

not detected even where the thermal model predicted its formation. Additional evidence of CO_2 and small amounts of H_2O frost where captured by HIRISE cameras (Gardin et al., 2010; Sinha and Ray, 2023) and Mars Express mission.

Unfortunately, there are no available quantitative data on water frost causing color changes on Mars, or sensitive polarization measurements of its surface. Nonetheless, some laboratory work has been carried out in the last years on frost deposition on Mars soil simulants observed in the visible spectrum. Pommerol et al. (2013) studied how frost deposited on top of JSC Mars-1 soil simulant affected its bidirectional reflectance at 650 nm. They found that a thin layer of frost increases the overall reflectance and enhances the forward scattering of the soil sample, although the experiment was limited to a single wavelength and incidence angle because of the rapid sublimation of the frost layer. Recently, Yoldi et al. (2021) carried out a spectral analysis of JSC Mars-1 soil simulant and dark basalt in association of different types of water ice, included frost. They observed that 100 μm of frost is enough to completely flatten the spectrum, making it indistinguishable from pure ice. This result agrees with our spectral slopes on MGS-1, which approach zero when the frost thickness approaches 100–150 μm (depending on the temperature of the regolith).

We note that frost growing on regolith samples does not change the reflectance spectrum in the same way as an intimate mixture of ice and regolith particles. Our data show an increase of reflectance in the blue when the frost is tens of microns thick, while an intimate mixture of spherical transparent ice particles and regolith produces the same effect only when larger quantities of ice are mixed within the dust (Yoldi et al., 2021). This is particularly important when the ice content is extrapolated by modeling the spectra of observational data — if the type of ice-dust association is unclear, the amount of ice could vary greatly depending on the mixing model. Furthermore, the surge of reflected blue light when a thin layer of frost forms on regolith provides a powerful advantage for recognizing it from other ice-dust associations.

The frost thickness or equivalent ice thickness retrieved from spectrophotometric data is a criterion that should be used carefully. In Fig. 7, we present the frost thickness measurements compared to the reflectance in the blue (R_{450}). At the beginning of our experiments, the frost thickness is increasing, since the frost dendrites expand outward from the regolith grain facelets. In this phase, the increase of thickness corresponds to an increase in reflectance too, and the frost thickness can be used effectively to track the reflectance changes that vary with the substrates and the frost deposition rate (i.e. the temperature of the sample for MGS-1). When the frost crystals grow up to approximately 100 μm, the frost on CR undergoes a stationary growth phase. The frost stops expanding outward from the grain surfaces, and grows between the preexisting ice crystals, increasing the density of the ice layer. This density increase of the frost layer corresponds to an increase in R_{450}. After this phase, large frost crystals (200–400 μm long) start to form on top of the regolith grains, and we stop the thickness analysis from the microscope images since the crystals evolve and collapse quickly under their weight, making it difficult to measure them precisely. The growth of large crystals corresponds to a decrease of reflectance at all wavelengths. The large ice crystals show a regular, transparent, elongated shape and the increase in transmissivity allows the photons to be absorbed in deeper layers of frost or to reach the dark substrate. This means that, at this stage, the visible reflectance no longer correlates with the frost thickness or the crystal size.

There is an important difference between our laboratory experiments and the frost depositing on Mars or on a cometary nucleus. In the first case, the cooling process happens from the bottom of the regolith sample, and the air above the sample has higher temperature than the sample itself, while in the second case the air temperature is lower than the regolith temperature. Since the growth of ice crystals is limited by their efficiency to disperse the latent heat of deposition, the heat transfer efficiency plays an important role in crystal growth (Kieffer, 1968).

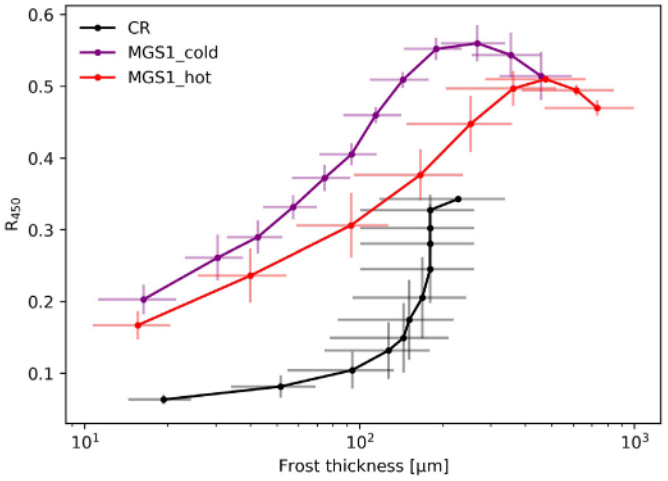

Fig. 7. The reflectance is the blue (R_{450}) plotted versus the frost thickness measured with the long-distance microscope for the different substrates. (For interpretation of the references to color in this figure legend, the reader is referred to the web version of this article.)

In the case of cooling below the sample, the ice crystals lose heat more efficiently through conduction to the cold regolith. This means that they tend to increase their width to maximize the contact with the cold regolith grains. In the case of an atmosphere colder than the surface, the deposited ice loses heat through radiation. This process is more efficient if the ice crystals are thin and elongated, to maximize their surface through which the heat is radiated to the atmosphere. This means that incident photons find more scatterers than in the case of wide shorter crystal, changing the overall spectrophotometric properties. Since it is not possible to reproduce the second case in our laboratory, we have to restrict our research to Earth-like frost. Knowing the differences with the extra-terrestrial frost, we can then extrapolate the expected spectral and polarimetric behavior. For the same frost thickness, the scattering within frost crystals in our experiments increases (i.e. the number density of the crystals on the regolith increases), we expect the regolith surface to become brighter more quickly, especially at shorter wavelengths. This means that the spectral slope would rapidly decrease as soon as the frost deposits, making it more detectable with spectral slopes calculated with $\lambda_1 = 450$ nm.

Often, the ice content on the substrates or intermixed with it is extrapolated by creating a synthetic spectrum from areal/intimate mixing of ice with the regolith dust. To obtain such a spectrum, the reflectance or single scattering albedo of ice and dust are linearly combined, and the ice amount is increased to fit the observed spectrum. From our data (Fig. 7), it is clear that this method can fail to reproduce a correct amount of ice whenever this layer comprises bigger translucent ice grains. On the other hand, a spectral linear mixing effectively detects an increase of amount of ice when the frost layer becomes denser (like in the case of CR in Fig. 7), since the reflectance increases too.

4.2. Multicolor polarimetry of growing frost

Only a few attempts at studying the linearly polarized reflected light from ice-dust associations have been made. This is mainly because of the scarcity of polarization instruments for planetary observations and the difficulty in interpreting the polarimetric data that are sensitive to many different parameters (hence also carrying a rich quantity of information). The linear polarization of deposited dust at small phase angles is dominated by multiple scattering within the grains composing the regolith. When the ice nucleation sites start to alter the multiple scattering on the surface, the polarization phase curve changes its shape. In general, frost forming on a black substratum moves the

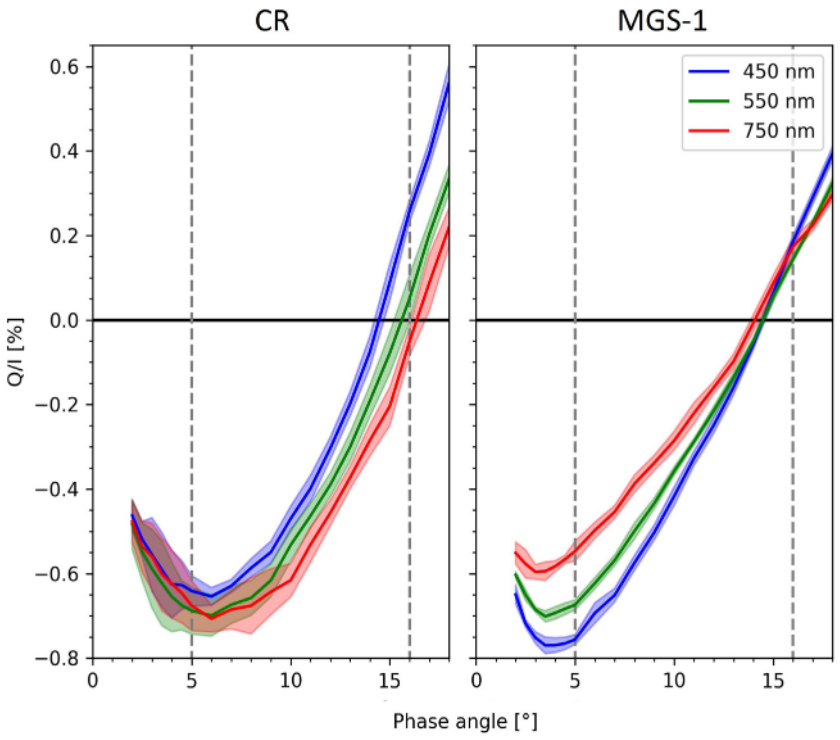

Fig. 8. Polarization phase curves of CR and MGS-1 simulants. The phase angles observed in our experiments are indicated with vertical dashed lines. (For interpretation of the references to color in this figure legend, the reader is referred to the web version of this article.)

minimum of the negative polarization to lower phase angles, whilst the inversion angle, α_{inv}, also decreases (see e.g. Poch et al. (2018)).

Before measuring the effect of frost on the regolith polarizance, we measured two polarimetric phase curves of the pristine room temperature regolith simulants, to compare them with the values at 5° and 16° of the frost deposition experiments. The acquisition procedure of these phase curves is slightly different compared to the one of the cryogenic samples, and is described in detail in Spadaccia et al. (2022). The regolith sample is placed on top of an azimuthal stage, which can rotate in steps of 45°. At each phase angle, the polarization is acquired for all three wavelengths and for five azimuthal steps between 0° and 360°. The azimuthal measurements are then averaged, so that the final result is not affected by the contribution of geometric effects.

During the frost deposition process, we measured the linear polarization signal at 5° and 16° because these values are close to the phase angle of the minimum polarization α_{min} and to the inversion angle of CR and MGS-1 (Fig. 8). Generally, if the linear polarization $|P_{5°}|$, increases, it means that $|P_{min}|$ is increasing, while its decrease means that the minimum polarization is moving toward smaller phase angles or the negative polarization becomes shallower. The measurement of the polarization at 16°, is used as a proxy to determine the position of the inversion angle α_{inv}. Since the polarization phase function is monotonically increasing between α_{min} and α_{max} (usually around 90–100° that is dependent on the Umov law), $P_{16°} > 0$ implies $\alpha_{inv} < 16°$, and $P_{16°} < 0$ means that the inversion angle moved to values $\alpha_{inv} > 16°$.

All our samples show a wavelength-dependent decrease of $P_{5°}$ when the first tens of micrometers of frost forms. At 5°, P_{450} shows the biggest decrease of the order of 0.25–0.5%, while P_{750} undergoes smaller changes of the order of 0.2%. When the first frost crystals are forming on the sample, blue light is Rayleigh scattered more efficiently, which increases the coherent backscattering opposition effect (CBOE). The CBOE is responsible for the surge of reflected negative polarization at small phase angles from regolith surfaces containing particles smaller than the observed wavelength (see Dlugach and Mishchenko (2013) and references therein). When small ice particles are introduced onto the regolith, the second order scattering between ice and regolith dust increases, thus increasing the probability of CBOE. The CBOE is more effective for second order scattering than higher order scattering, and there is a point when the surface is covered by sufficient ice particles to produce higher order multiple scattering across the surface, scrambling the linear polarization and decreasing its overall averaged signal. This is the reason why, when the frost becomes thick enough and it hides the regolith beneath, the linear polarization decreases to zero without any wavelength dependence. Note that the minimum of P_{450} is reached when the frost is tens of microns thick. This means that such a thickness of small crystals is still allowing an efficient second order scattering between ice and dust grains.

At 16°, the linear polarization is also wavelength dependent, although it depends on the sample and its temperature. CR shows an interesting α_{inv} behavior. When the frost is approximately 30–50 µm thick, P_{750} becomes positive, while P_{450} reaches its minimum at $P_{450} \sim$ –0.5%. This means that the 450 nm polarization phase curve increases its α_{inv} by several degrees, while the 750 nm polarization phase curve decreases its inversion angle. This is very different from the starting inversion angles of the initially pure CR (see Fig. 8 left).

The polarization phase curve of the dry MGS-1 soil simulant does not show a particular dependence of α_{inv} on wavelength (see Fig. 8 right). For the cold case MGS-1 ($T_{min} = -130$ °C), P_{450} and P_{550} at 16° show a certain degree of variability between experiments, and a clear distinction between the wavelengths is not possible. However, both P_{450} and P_{550} shift from positive to negative values when the frost is 10–20 µm thick, meaning that the inversion angle slightly increases. The hot MGS-1 ($T_{min} = -100$ °C) shows a completely different evolution at 16°. P is positive at all wavelengths for the entire experiment duration. While P_{750} slightly increases over time, P_{450} increases sharply from $P_{450} = 0.15\%$ to $P_{450} = 0.45\%$ when frost thickness is approximately 20 µm. Note that the P_{450} surge does not correspond necessarily to a decrease of inversion angle, P_{min} of MGS-1 can deepen maintaining the same inversion angle (approximately $\alpha_{inv} = 14°$) and causing the increase of P at 16°.

The two experiments with MGS-1 at different temperatures consist of three experimental repetitions, each performed with a new pristine regolith sample. Eventual differences in roughness and particle

size distribution of each regolith sample are not sufficient to change significantly the starting polarization measurement, resulting in small standard deviations at the beginning of the two experiments (less than 0.05%). Since the only other difference between the two experiments with MGS-1 is the regolith temperature, the difference in polarization at 16° must be related to some temperature dependent property of the frost. The two temperatures chosen for the experiments are close to the crystalline structure transitions for ice at ambient pressure (Kumai, 1968). However, at the present time, there are no specific studies on the polarizance of ice with different crystalline structures. At T= −130 °C to −100 °C both cubic and hexagonal ice can form, but as soon as the temperature rises above −100 °C only hexagonal ice can form. The reflectance of the two types of frost are different in the blue, with higher reflectance for the frost formed at T= −130 °C to −100 °C (Fig. 7). The scattering properties of the ice can be a result of its type of crystalline macrostructures (like the shape of dendrites growing on the regolith) or the single cubic or hexagonal ice crystals, that have different single-scattering properties (Riikonen et al., 2000). The negative polarization phase curve of MGS-1 at 450 nm seems to widen and deepen slightly when the first tens of micrometers of deposited frost has a mixed cubic/hexagonal structure, while for only hexagonal ice frost a greater decrease of P_{min} with no α_{inv} increase is observed.

4.3. Effect of the first micrometers of frost

In Fig. 8 we can see that the expected CR polarization in the blue at 16° is $P_{450} = 0.25\%$. This is not the measured polarization when we start our frost deposition experiment (Fig. 4), that is $P_{450} = -0.1\%$. The blue polarization value decreased in the time between the start of the experiment and when we start to acquire the data. To some extent, this is true also for the polarization at 550 nm, although the difference is almost within the uncertainty. This effect can be explained by a thin frost film formed before acquiring the measurement. In our experiments, we insert an aluminum lid over the sample before starting to cool down the cryo-stage, when the POLICES enclosure still contains ambient air. Some of that air remains trapped between the sample and the lid and might deposit over the sample as soon as it becomes cold enough and before acquiring the first polarization data. To prove that this effect is due to some frost deposition, we repeated an experiment with CR without placing the lid at the beginning of the cooling phase (Fig. 9). The experiment was performed only at 450 nm since this wavelength is mostly affected. It takes about 10 min to lower the temperature of the regolith from room temperature to 0 °C, and in the meanwhile the enclosure is completely flushed with nitrogen. When the regolith temperature decreases below the freezing point, the air is virtually absent in the chamber, and frost cannot form. In Fig. 9 we can see that the regolith sample not covered by the lid maintains a constant reflected polarized and total light even when the temperature drops to −100 °C. After 25 min, the nitrogen flushing is stopped. In about seven minutes, the polarization drops from $P_{450} = 0.25\%$ to negative values, and the reflectance starts increasing by approximately 0.2%. This is a clear sign of frost deposition happening on the sample.

It is difficult to measure directly the thickness of this first frost deposition, since there is no difference between the images taken with the microscope before starting the experiment and when we start measuring the reflected light (i.e. after the cooling phase). A rough lower limit of frost thickness can be calculated from the amount of moisture that is trapped above the sample. Since the relative humidity in the laboratory is usually approximately 40% and knowing the volume of air trapped over the sample, if we assume that all the water deposits as ice on the sample, the thickness should be ∼1 μm. This supports the fact that a thin layer of frost is forming on the sample and interacts with the blue light, giving rise to a change of polarization and a slight increase in reflectance. The polarization phase curves of MGS-1 are in good agreement with the linear polarization measured at the beginning of the experiments at 5° and 16°. This means that either we do not form any thin ice film, or the ice film is not optically thick in the blue. Since frost deposits slower on MGS-1 than on CR, it might be that the vapor pressure needed to start the ice nucleation is higher than just the saturation pressure at that temperature, causing a delay in the formation of such a thin layer, which forms more rapidly as soon as ambient air is allowed to enter the enclosure.

5. Perspectives for remote sensing and future experiments

Our experiments are limited to very specific geometries, with the linear polarization measured at phase angles 5° or 16°, and the reflected total intensity at 50° and 66°. In the right conditions of water vapor pressure and temperature, frost forms on planetary surfaces, and these conditions are often met in shadowed areas (at terminators, or close to cliffs and on crater slopes). For instance, in the case of 67P the observation of ice patches in the Anhur/Bes regions occurred at phase angles $\alpha = 61°–75°$ that are very similar to our experimental conditions for the total light measurements. The uncertainty related to the spectral slope measurements on 67P is small enough to detect the small changes due to tens of microns of deposited frost, showing that *Rosetta* Optical, Spectroscopic, and Infrared Remote Imaging System (OSIRIS) design can be applied successfully to other missions for frost and ice detection.

The shadowed regions were in that case caused by the irregular topography of the region and the presence of cliffs and steep scarps. On Mars, nighttime frost is often observed in crater shadows, that are best observed at larger phase angles. Conversely, the negative polarization must be observed with phase angles up to the inversion angle of the observed regolith (in the range $\alpha_{inv} = 15°–25°$ for most planetary surfaces). This means that to observe shadow-rich regions like the terminator, both the incidence angle and the emission angle (where the observer is) must be large, which requires that either the telescope or the spacecraft specifically maneuver to target those areas (Fig. 10). On the other hand, if we observe frost on shadowed slopes or cliffs, the emission angle constraint can be relaxed, depending on the slope angle and the incidence of the sunlight.

Since it was demonstrated that the negative polarization can contribute to determining the compositional properties, porosity, grain shape and grain size of regolith-like materials (see for instance Shkuratov and Ovcharenko (2002), Escobar-Cerezo et al. (2018), Frattin et al. (2019) and Spadaccia et al. (2022)), polarimeters should be considered a very useful addition to onboard imaging instrumentation of future planetary missions. Polarimeters could be exploited also on rovers and landers, that have more freedom in observing at high emission angles, and in-situ frost formation and evolution. Furthermore, having polarization cameras on rovers or landers is of great interest for studying the properties of aerosols and atmospheric dust and clouds.

The main limitation for frost and ice detection through polarimetry is the current lack of high-precision instruments considered for planetary missions. Many past planetary missions carried polarimeters of different types used to image other Solar System bodies. The first missions to have polarimeters were the *Pioneer* 10 and 11 spacecrafts, launched in 1972 and 1973, respectively. Their imaging photopolarimeters (IPP) provided the first in situ polarization images of Jupiter and Titan (Coffeen, 1974; Baker et al., 1975; Tomasko and Smith, 1982). In 1977, *Voyager* 1 and 2 were launched, carrying both a photopolarimeter subsystem (PPS). Only *Voyager* 2 managed to acquire polarization data though, since the PPS of *Voyager* 1 experienced a quick degradation due to the harsh space environment. IPP polarization uncertainty was ±0.5% and allowed the first polarization observation of the equatorial zone of Saturn polarization at 264 nm and 750 nm (West et al., 1983). In 1986 and 1990 the *Giotto*'s optical probe experiment (OPE) measured successfully the linear polarization signal of comet 1P/Halley (Levasseur-Regourd et al., 1985) and of comet Grigg-Skjellerup (Levasseur-Regourd et al., 1993) comae with a sensitivity of 0.5–1%. In the meanwhile, the *Galileo* spacecraft was launched in 1989 and its Photopolarimeter/Radiometer (PPR) experiment (Russell

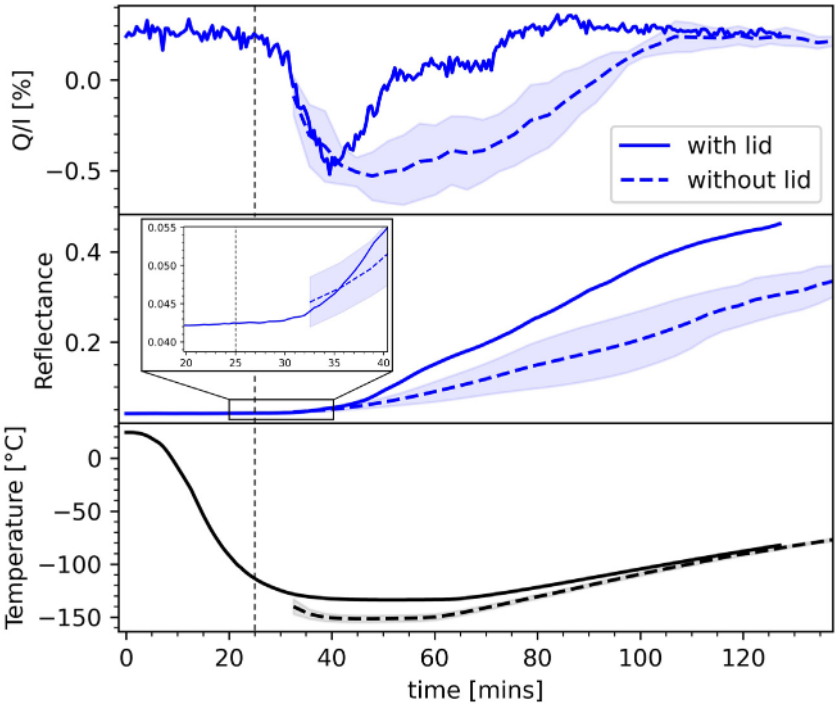

Fig. 9. The linear polarization and reflectance of CR at 450 nm and $\alpha = 16°$. The continuous line represents one experiment without the lid over the sample, while the blue dashed line represents the average of the experiments conducted with the lid over the sample during the cooling phase (see Fig. 4). The black vertical dashed line represents the time at which the nitrogen flushing is stopped. On the bottom, the temperatures of the sample in the case with and without lid are plotted versus time. (For interpretation of the references to color in this figure legend, the reader is referred to the web version of this article.)

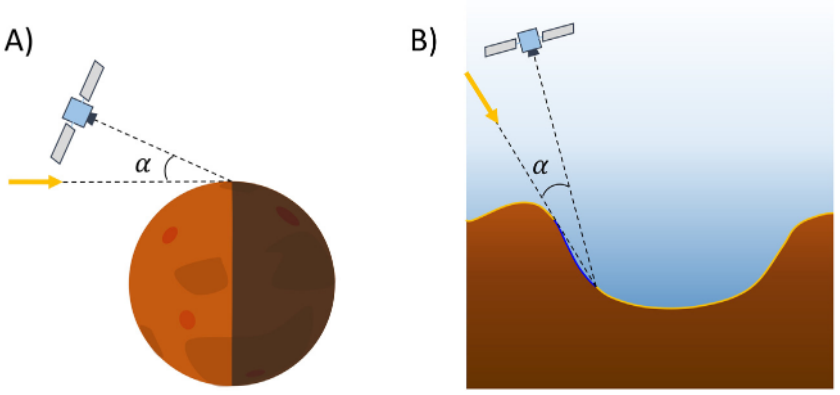

Fig. 10. Possible geometries to measure negative polarization of frost though remote sensing. (A) the terminator is rich in shadows and is the perfect area where to search for frost, but this requires high observation angles to remain at small phase angles. (B) Craters and local topographic features allow relaxing the observation angle of the spacecraft, always remaining at small phase angles to observe the reflected negative polarization in shadowed areas (indicated with a blue line on the left crater wall).

et al., 1992) started to acquire linear polarization data of Jupiter and its moons with uncertainties down to ±0.3% (Braak et al., 2002). More recently, the Imaging Science Subsystem (ISS) of *Cassini* acquired polarization images of Saturn and its moons using a narrow angle camera (NAC) and a wide angle camera (WAC) equipped with different filters in the range 350–1100 nm (Porco et al., 2004). The two cameras have two filter wheels in front of their main aperture, allowing a coupling of pass-band filters and NIR and VIS polarizers. Unfortunately, there are not published works on the polarization data of ISS, although the sensitivity of the instrument is expected to be ±0.5% in linear polarization (Porco et al., 2004).

The linear polarization uncertainty of the aforementioned instruments hides the most fine features of the negative polarization of regolith surfaces that requires uncertainties down to the order of 0.1%. Although previous planetary mission polarization instruments do not meet this requirement and there are no other planned polarimeters in the near-future planetary missions, some high-accuracy spectropolarimeter designs for Earth observation already exist. For instance, the Aerosol Polarimetry Sensor (APS) on board of NASA Glory satellite was designed for observing Earth atmosphere degree of polarization with uncertainties of about 0.2%, but unfortunately the Glory mission failed during the launch phase in 2011 (Knobelspiesse et al., 2012). More recently, the Lunar Observatory for Unresolved Polarimetry of the Earth (LOUPE) targets polarization uncertainties lower than 0.1%, to observe Earth as an exoplanet from the Moon (Klindžić et al., 2021). Future Earth observation missions will demonstrate the feasibility and usefulness of high-accuracy polarimetric data, possibly paving the way toward future polarimetry mission for exploring our Solar System.

Future experiments should include different types of deposited ices (CO_2, SO_2) commonly found in our Solar System, together with other regolith simulants and organics. While the NIR and IR spectral behaviors of different types of water ice and dust associations have already

been investigated (Pommerol et al., 2013; Yoldi et al., 2021), the NIR negative polarization is poorly studied. The reflected negative polarization at the ice NIR absorption bands is particularly interesting, since the reflectance of frost drops significantly, and this can lead to an increase of negative polarization when mixed with higher albedo dust (the mixing effect described in Shkuratov (1989) and Spadaccia et al. (2022). We would like to notice that there are no experimental studies of the positive part of the polarization phase curve of icy surfaces. Future experiments could, in addition to the small phase angles, also measure the polarization at larger angles in order to retrieve the whole polarization phase curve of regolith simulants covered by ice.

6. Conclusions

We have experimentally investigated the reflected polarized and total light from water frost forming on regolith simulant at different visible wavelengths, correlating the spectral slope and the linear polarization to the measured properties of the frost (thickness, temperature and crystal shape). We found that early frost formation changes the reflected blue light and the multiple scattering within the surface grains rapidly, causing a surge in negative polarization and an increase of reflected light. The spectral slope calculated between 450–550 nm and the difference between the negative polarization at small phase angles at 450 nm and 750 nm are sensitive in detecting thin frost layers. This makes frost detection possible when the frost is only 10–20 μm thick. The polarization measured close to the inversion phase angle shows different behavior with respect to the temperature of the regolith simulant, and it seems correlated to the phase transition from the cubic to the hexagonal ice crystal structure. Finally, our measured frost thickness agrees with the frost thickness derived by thermal modeling on some regions of 67P. We can compare the efficiency of spectral slope and negative polarization observation of frost deposited on regolith as follows:

- the visible spectral slope varies quickly when frost deposits if calculated using $\lambda = 450$ nm as smaller wavelength. After the first 30–50 μm of deposited frost, the spectral slope evolves more slowly, as ice crystals grow bigger. While spectral slope can provide good measurements of frost depositing on dark regolith, its variation over time is not sensitive to the temperature of the regolith;
- negative polarization measured at phase angles close to the minimum of polarization and the inversion angle, with a blue ($\lambda = 450$ nm) and red filter ($\lambda = 750$ nm) provides very good sensitivity to the first micrometers of frost formed on the substrate, but requires high precision (down to 0.1% measurement error). Furthermore, polarization measurements are sensitive to the temperature at which the frost is deposited. We interpret this as a sensitivity to its crystalline structure (cubic or hexagonal).

In conclusion, both techniques provide useful and precise information on frost thickness over time, and negative polarization can add information on the crystal structure of ice at the cost of a higher sensitivity requirement. These results are of paramount importance to extrapolate water frost physical properties from remote-sensing data, giving a better insight on ice deposition and evolution processes on surfaces of Solar System bodies. This data set will be extended for other ices, regolith substrates, and observed wavelengths with future experiments in the Icelab at the University of Bern.

CRediT authorship contribution statement

Stefano Spadaccia: Conceptualization, Methodology, Investigation, Data curation, Formal analysis, Visualization, Writing – original draft. **C.H. Lucas Patty:** Conceptualization, Investigation, Methodology, Supervision, Validation, Writing – review & editing. **Nicolas Thomas:** Supervision, Validation, Writing – review & editing. **Antoine Pommerol:** Conceptualization, Project administration, Resources, Supervision, Validation, Writing – review & editing.

Data availability

The polarimetric data can be found on Zenodo: https://doi.org/10.5281/zenodo.7681502.

References

A'Hearn, M.F., Belton, M.J., Delamere, W.A., Feaga, L.M., Hampton, D., Kissel, J., Klaasen, K.P., McFadden, L.A., Meech, K.J., Melosh, H.J., et al., 2011. EPOXI at comet Hartley 2. Science 332 (6036), 1396–1400.

Baker, A., Baker, L., Beshore, E., Blenman, C., Castillo, N., Chen, Y.-P., Doose, L., Elston, J., Fountain, J., Gehrels, T., et al., 1975. The imaging photopolarimeter experiment on Pioneer 11. Science 188 (4187), 468–472.

Beck, P., Quirico, E., Sevestre, D., Montes-Hernandez, G., Pommerol, A., Schmitt, B., 2011. Goethite as an alternative origin of the 3.1 μm band on dark asteroids. Astron. Astrophys. 526, A85.

Belskaya, I., Cellino, A., Levasseur-Regourd, A.-C., Bagnulo, S., 2019. Optical Polarimetry of Small Solar System Bodies: From Asteroids to Debris Disks. In: Mignani, R., Shearer, A., Słowikowska, A., Zane, S. (Eds.), Astronomical Polarisation from the Infrared To Gamma Rays. In: Astrophysics and Space Science Library, Springer International Publishing, Cham, pp. 223–246. http://dx.doi.org/10.1007/978-3-030-19715-5_9.

Belskaya, I., Fornasier, S., Tozzi, G., Gil-Hutton, R., Cellino, A., Antonyuk, K., Krugly, Y.N., Dovgopol, A., Faggi, S., 2017. Refining the asteroid taxonomy by polarimetric observations. Icarus 284, 30–42.

Blum, J., Bischoff, D., Gundlach, B., 2022. Formation of comets. Universe 8 (7), 381.

Braak, C., De Haan, J., Hovenier, J., Travis, L., 2002. Galileo photopolarimetry of Jupiter at 678.5 nm. Icarus 157 (2), 401–418.

Britt, D.T., Cannon, K.M., Donaldson Hanna, K., Hogancamp, J., Poch, O., Beck, P., Martin, D., Escrig, J., Bonal, L., Metzger, P.T., 2019. Simulated asteroid materials based on carbonaceous chondrite mineralogies. Meteorit. Planet. Sci. 54 (9), 2067–2082.

Campins, H., Hargrove, K., Pinilla-Alonso, N., Howell, E.S., Kelley, M.S., Licandro, J., Mothé-Diniz, T., Fernández, Y., Ziffer, J., 2010. Water ice and organics on the surface of the asteroid 24 Themis. Nature 464 (7293), 1320–1321.

Cannon, K.M., Britt, D.T., Smith, T.M., Fritsche, R.F., Batcheldor, D., 2019. Mars global simulant MGS-1: A rocknest-based open standard for basaltic martian regolith simulants. Icarus 317, 470–478.

Carrozzo, F., Bellucci, G., Altieri, F., D'aversa, E., Bibring, J.-P., 2009. Mapping of water frost and ice at low latitudes on Mars. Icarus 203 (2), 406–420.

Cellino, A., Gil-Hutton, R., Belskaya, I., 2015. Asteroids. In: Levasseur-Regourd, A.-C., Hough, J., Kolokolova, L. (Eds.), Polarimetry of Stars and Planetary Systems. Cambridge University Press, Cambridge, pp. 360–378. http://dx.doi.org/10.1017/CBO9781107358249.021, URL: https://www.cambridge.org/core/books/polarimetry-of-stars-and-planetary-systems/asteroids/9EE5970462DD0D283F6A861B4DA60298.

Clark, R.N., 1981. The spectral reflectance of water-mineral mixtures at low temperatures. J. Geophys. Res.: Solid Earth 86 (B4), 3074–3086.

Coffeen, D.L., 1974. Optical polarimeters in space. In: Colloquium on the Planets, Stars and Nebulae Studied with Photopolarimetry.

De Sanctis, M.C., Capaccioni, F., Ciarniello, M., Filacchione, G., Formisano, M., Mottola, S., Raponi, A., Tosi, F., Bockelée-Morvan, D., Erard, S., et al., 2015. The diurnal cycle of water ice on comet 67P/Churyumov–Gerasimenko. Nature 525 (7570), 500–503.

Delsanti, A., Boehnhardt, H., Barrera, L., Meech, K., Sekiguchi, T., Hainaut, O., 2001. Photometry of 27 kuiper belt objects with ESO/Very large telescope. Astron. Astrophys. 380 (1), 347–358.

Dlugach, Z.M., Mishchenko, M., 2013. Coherent backscattering and opposition effects observed in some atmosphereless bodies of the solar system. Sol. Syst. Res. 47 (6), 454–462.

Dollfus, A., 1957. Étude des planètes par la polarisation de leur lumière. Suppl. Ann. D'Astrophys. 4, 3–114.

Dollfus, A., 1998. Lunar surface imaging polarimetry: I. Roughness and grain size. Icarus 136 (1), 69–103.

Escobar-Cerezo, J., Muñoz, O., Moreno, F., Guirado, D., Martín, J.C.G., Goguen, J.D., Garboczi, E.J., Chiaramonti, A.N., Lafarge, T., West, R.A., 2018. An Experimental Scattering Matrix for Lunar Regolith Simulant JSC-1A at Visible Wavelengths. Astrophys. J. Suppl. 235 (1), 19. http://dx.doi.org/10.3847/1538-4365/aaa6cc, URL: https://doi.org/10.3847/1538-4365/aaa6cc, Publisher: American Astronomical Society.

Fornasier, S., Feller, C., Hasselmann, P.H., Barucci, M.A., Sunshine, J., Vincent, J.-B., Shi, X., Sierks, H., Naletto, G., Lamy, P., et al., 2019. Surface evolution of the anhur region on comet 67P/Churyumov-Gerasimenko from high-resolution OSIRIS images. Astron. Astrophys. 630, A13.

Fornasier, S., Hasselmann, P.H., Barucci, M., Feller, C., Besse, S., Leyrat, C., Lara, L., Gutiérrez, P.J., Oklay, N., Tubiana, C., et al., 2015. Spectrophotometric properties of the nucleus of comet 67P/Churyumov-Gerasimenko from the OSIRIS instrument onboard the ROSETTA spacecraft. Astron. Astrophys. 583, A30.

Fornasier, S., de Micas, J.B., Hasselmann, P.H., Hoang, H., Barucci, M.A., Sierks, H., 2021. Small lobe of comet 67P: Characterization of the wosret region with ROSETTA-OSIRIS. Astron. Astrophys. 653, A132.

Fornasier, S., Mottola, S., Keller, H.U., Barucci, M., Davidsson, B., Feller, C., Deshapriya, J., Sierks, H., Barbieri, C., Lamy, P., et al., 2016. Rosetta's comet 67P/Churyumov-Gerasimenko sheds its dusty mantle to reveal its icy nature. Science 354 (6319), 1566–1570.

Frattin, E., Muñoz, O., Moreno, F., Nava, J., Escobar-Cerezo, J., Martin, J.C.G., Guirado, D., Cellino, A., Coll, P., Raulin, F., Bertini, I., Cremonese, G., Lazzarin, M., Naletto, G., La Forgia, F., 2019. Experimental phase function and degree of linear polarization of cometary dust analogs. Mon. Not. R. Astron. Soc. 484 (2), 2198–2211. http://dx.doi.org/10.1093/mnras/stz129, URL: http://arxiv.org/abs/1901.05975 arXiv:1901.05975.

Gardin, E., Allemand, P., Quantin, C., Thollot, P., 2010. Defrosting, dark flow features, and dune activity on Mars: Example in Russell crater. J. Geophys. Res.: Planets 115 (E6).

Iraci, L.T., Phebus, B.D., Stone, B.M., Colaprete, A., 2010. Water ice cloud formation on mars is more difficult than presumed: Laboratory studies of ice nucleation on surrogate materials. Icarus 210 (2), 985–991.

Jewitt, D., Guilbert-Lepoutre, A., 2011. Limits to ice on asteroids (24) Themis and (65) Cybele. Astron. J. 143 (1), 21.

Jones, K.L., Arvidson, R.E., Guinness, E.A., Bragg, S.L., Wall, S.D., Carlston, C.E., Pidek, D.G., 1979. One Mars year: Viking lander imaging observations. Science 204 (4395), 799–806.

Kemp, J.C., Henson, G., Steiner, C., Powell, E., 1987. The optical polarization of the Sun measured at a sensitivity of parts in ten million. Nature 326 (6110), 270–273.

Kieffer, H.H., 1968. Near Infrared Spectral Reflectance of Simulated Martian Frosts (Ph.D. thesis). California Institute of Technology.

Klindžić, D., Stam, D.M., Snik, F., Keller, C., Hoeijmakers, H., van Dam, D., Willebrands, M., Karalidi, T., Pallichadath, V., van Dijk, C., et al., 2021. LOUPE: observing earth from the moon to prepare for detecting life on earth-like exoplanets. Phil. Trans. R. Soc. A 379 (2188), 20190577.

Knobelspiesse, K., Cairns, B., Mishchenko, M., Chowdhary, J., Tsigaridis, K., van Diedenhoven, B., Martin, W., Ottaviani, M., Alexandrov, M., 2012. Analysis of fine-mode aerosol retrieval capabilities by different passive remote sensing instrument designs. Opt. Express 20 (19), 21457–21484.

Kumai, M., 1968. Hexagonal and cubic ice at low temperatures. J. Glaciol. 7 (49), 95–108.

Levasseur-Regourd, A.-C., Agarwal, J., Cottin, H., Engrand, C., Flynn, G., Fulle, M., Gombosi, T., Langevin, Y., Lasue, J., Mannel, T., et al., 2018. Cometary dust. Space Sci. Rev. 214 (3), 1–56.

Levasseur-Regourd, A.-C., Bertaux, J.-L., Le Blanc, J., Weinberg, J., Giovane, F., Dumont, R., Festou, M., Giese, R., Lamy, P., Llebaria, A., 1985. In-situ photopolarimetric measurements of dust and gas in the coma of Halley's comet. Adv. Space Res. 5 (12), 197–199.

Levasseur-Regourd, A., Goidet, B., Le Duin, T., Malique, C., Renard, J., Bertaux, J., 1993. Optical probing of dust in comet Grigg-Skjellerup from the Giotto spacecraft. Planet. Space Sci. 41 (2), 167–169.

Li, J.-Y., A'Hearn, M.F., Belton, M.J., Crockett, C.J., Farnham, T.L., Lisse, C.M., McFadden, L.A., Meech, K.J., Sunshine, J.M., Thomas, P.C., et al., 2007. Deep impact photometry of comet 9P/Tempel 1. Icarus 187 (1), 41–55.

Li, J.-Y., Besse, S., A'Hearn, M.F., Belton, M.J., Bodewits, D., Farnham, T.L., Klaasen, K.P., Lisse, C.M., Meech, K.J., Sunshine, J.M., et al., 2013. Photometric properties of the nucleus of Comet 103P/Hartley 2. Icarus 222 (2), 559–570.

Liao, Y., Marschall, R., Su, C., Wu, J.-S., Lai, I., Pinzon, O., Thomas, N., 2018. Water vapor deposition from the inner gas coma onto the nucleus of comet 67P/Churyumov-Gerasimenko. Planet. Space Sci. 157, 1–9.

Licandro, J., Campins, H., Tozzi, G., De Léon, J., Pinilla-Alonso, N., Boehnhardt, H., Hainaut, O., 2011. Testing the comet nature of main belt comets. The spectra of 133P/Elst-Pizarro and 176P/LINEAR. Astron. Astrophys. 532, A65.

Lv, Y., Sun, Z., 2014. The reflectance and negative polarization of light scattered from snow surfaces with different grain size in backward direction. J. Quant. Spectrosc. Radiat. Transfer 133, 472–481.

O'rourke, L., Müller, T.G., Biver, N., Bockelée-Morvan, D., Hasegawa, S., Valtchanov, I., Küppers, M., Fornasier, S., Campins, H., Fujiwara, H., et al., 2020. Low water outgassing from (24) themis and (65) cybele: 3.1 μm near-IR spectral implications. Astrophys. J. Lett. 898 (2), L45.

Patty, C.H.L., Pommerol, A., Kuehn, J., Demory, B., Thomas, N., 2022. Directional aspects of vegetation linear and circular polarization biosignatures. Astrobiology 22 (9), http://dx.doi.org/10.1089/ast.2021.0156.

Poch, O., Cerubini, R., Pommerol, A., Jost, B., Thomas, N., 2018. Polarimetry of water ice particles providing insights on grain size and degree of sintering on icy planetary surfaces. J. Geophys. Res.: Planets 123 (10), 2564–2584. http://dx.doi.org/10.1029/2018je005753.

Pommerol, A., Jost, B., Poch, O., Yoldi, Z., Brouet, Y., Gracia-Berná, A., Cerubini, R., Galli, A., Wurz, P., Gundlach, B., et al., 2019. Experimenting with mixtures of water ice and dust as analogues for icy planetary material. Space Sci. Rev. 215 (5), 1–68.

Pommerol, A., Thomas, N., El-Maarry, M.R., Pajola, M., Groussin, O., Auger, A.-T., Oklay, N., Fornasier, S., Feller, C., Davidsson, B., et al., 2015. OSIRIS observations of meter-sized exposures of H2O ice at the surface of 67P/Churyumov-Gerasimenko and interpretation using laboratory experiments. Astron. Astrophys. 583, A25.

Pommerol, A., Thomas, N., Jost, B., Beck, P., Okubo, C., McEwen, A., 2013. Photometric properties of Mars soils analogs. J. Geophys. Res.: Planets 118 (10), 2045–2072.

Porco, C.C., West, R.A., Squyres, S., McEwen, A., Thomas, P., Murray, C.D., Delgenio, A., Ingersoll, A.P., Johnson, T.V., Neukum, G., et al., 2004. Cassini imaging science: Instrument characteristics and anticipated scientific investigations at Saturn. Space Sci. Rev. 115 (1), 363–497.

Raponi, A., Ciarniello, M., Capaccioni, F., Filacchione, G., Tosi, F., De Sanctis, M.C., Capria, M., Barucci, M., Longobardo, A., Palomba, E., et al., 2016. The temporal evolution of exposed water ice-rich areas on the surface of 67P/Churyumov–Gerasimenko: Spectral analysis. Mon. Not. R. Astron. Soc. 462 (Suppl_1), S476–S490.

Riikonen, M., Sillanpää, M., Virta, L., Sullivan, D., Moilanen, J., Luukkonen, I., 2000. Halo observations provide evidence of airborne cubic ice in the Earth's atmosphere. Appl. Opt. 39 (33), 6080–6085.

Rivkin, A.S., Emery, J.P., 2010. Detection of ice and organics on an asteroidal surface. Nature 464 (7293), 1322–1323.

Roush, T., Pollack, J., Witteborn, F., Bregman, J., Simpson, J., 1990. Ice and minerals on Callisto: A reassessment of the reflectance spectra. Icarus 86 (2), 355–382.

Russell, E., Brown, F., Chandos, R., Fincher, W., Kubel, L., Lacis, A., Travis, L., 1992. Galileo photopolarimeter/radiometer experiment. Space Sci. Rev. 60 (1), 531–563.

Schorghofer, N., 2016. Predictions of depth-to-ice on asteroids based on an asynchronous model of temperature, impact stirring, and ice loss. Icarus 276, 88–95.

Schorghofer, N., Edgett, K.S., 2006. Seasonal surface frost at low latitudes on Mars. Icarus 180 (2), 321–334.

Shkuratov, I.G., 1989. A new mechanism for the negative polarization of light scattered by the solid surfaces of cosmic bodies. Astron. Vestn. 23, 176–180.

Shkuratov, Y.G., Ovcharenko, A., 2002. Polarization of light scattered by surfaces with complex microstructure at phase angles 0.1–3.5. Sol. Syst. Res. 36 (1), 62–67.

Shkuratov, Y., Ovcharenko, A., Zubko, E., Miloslavskaya, O., Muinonen, K., Piironen, J., Nelson, R., Smythe, W., Rosenbush, V., Helfenstein, P., 2002. The Opposition Effect and Negative Polarization of Structural Analogs for Planetary Regoliths. Icarus 159 (2), 396–416. http://dx.doi.org/10.1006/icar.2002.6923, URL: https://www.sciencedirect.com/science/article/pii/S001910350296923X.

Sinha, R.K., Ray, D., 2023. Morphological changes currently occurring in sand-filled gully channels on Mars: Implications for the role of substrates inside channels. Icarus 390, 115334.

Smith, P.H., Tamppari, L., Arvidson, R., Bass, D., Blaney, D., Boynton, W.V., Carswell, A., Catling, D., Clark, B., Duck, T., et al., 2009. H2O at the Phoenix landing site. Science 325 (5936), 58–61.

Spadaccia, S., Patty, C., Capelo, H.L., Thomas, N., Pommerol, A., 2022. Negative polarization properties of regolith simulants-systematic experimental evaluation of composition effects. Astron. Astrophys. 665, A49.

Steigmann, G., 1993. The two faces of Callisto. Observatory 113, 70–74.

Sunshine, J., A'hearn, M., Groussin, O., Li, J.-Y., Belton, M., Delamere, W., Kissel, J., Klaasen, K., McFadden, L., Meech, K., et al., 2006. Exposed water ice deposits on the surface of comet 9P/Tempel 1. Science 311 (5766), 1453–1455.

Svitek, T., Murray, B., 1990. Winter frost at Viking Lander 2 site. J. Geophys. Res.: Solid Earth 95 (B2), 1495–1510.

Tomasko, M.G., Smith, P.H., 1982. Photometry and polarimetry of titan: Pioneer 11 observations and their implications for aerosol properties. Icarus 51 (1), 65–95.

West, R., Sato, M., Hart, H., Lane, A., Hord, C., Simmons, K., Esposito, L., Coffeen, D., Pomphrey, R., 1983. Photometry and polarimetry of saturn at 2640 and 7500 Å. J. Geophys. Res. Space Phys. 88 (A11), 8679–8697.

Yang, B., Jewitt, D., 2007. Spectroscopic search for water ice on Jovian Trojan asteroids. Astron. J. 134 (1), 223.

Yoldi, Z., Pommerol, A., Poch, O., Thomas, N., 2021. Reflectance study of ice and mars soil simulant associations–I. H2O ice. Icarus 358, 114169.

Zubko, E., Muinonen, K., Muñoz, O., Nousiainen, T., Shkuratov, Y., Sun, W., Videen, G., 2013. Light scattering by feldspar particles: Comparison of model agglomerate debris particles with laboratory samples. J. Quant. Spectrosc. Radiat. Transfer 131, 175–187. http://dx.doi.org/10.1016/j.jqsrt.2013.01.017, URL: https://www.sciencedirect.com/science/article/pii/S0022407313000368.